AGU
ADVANCING EARTH AND SPACE SCIENCE

Radio Science®

Key Points:

- Meteoroid trajectory and speed determined with a continuous wave forward scatter radio set-up
- Trajectory reconstruction solver is validated against simulated data but the problem is ill-conditioned
- Interferometry required for an accuracy of <10% on the velocity and <2° on the inclination for most trajectories

Correspondence to:
J. Balis,
joachim.balis@aeronomie.be

Reconstructing Meteoroid Trajectories Using Forward Scatter Radio Observations From the BRAMS Network

Joachim Balis[1,2] , **Hervé Lamy[1]** , **Michel Anciaux[1]** , and **Emmanuel Jehin[2]**

[1]Royal Belgian Institute for Space Aeronomy, Brussels, Belgium, [2]STAR Institute, University of Liège, Liège, Belgium

Abstract In this paper, we aim to reconstruct meteoroid trajectories using a forward scatter radio system transmitting a continuous wave (CW) with no modulation. To do so, we use the meteor echoes recorded at the receivers of the BRAMS (Belgian RAdio Meteor Stations) network. This system consists, at the time of writing, of a dedicated transmitter and 44 receiving stations located in and nearby Belgium, all synchronized using GPS clocks. Our approach processes the meteor echoes at the BRAMS receivers and uses the time delays as inputs to a nonlinear optimization solver. We compare the quality of our reconstructions with and without interferometric data to the trajectories given by the optical CAMS (Cameras for Allsky Meteor Surveillance) network in Benelux. We show that the general CW forward scatter trajectory reconstruction problem can be solved, but we highlight its strong ill-conditioning. With interferometry, this high sensitivity to the inputs is alleviated and the reconstructed trajectories are in good agreement with optical ones, displaying an uncertainty smaller than 10% on the velocity and 2° on the inclination for most cases. To increase accuracy, the trajectory reconstruction with time delays only should be complemented by information about the signal phase. The use of at least one interferometer makes the problem much easier to solve and greatly improves the accuracy of the retrieved velocities and inclinations. Increasing the number of receiving stations also enhances the quality of the reconstructions.

Plain Language Summary This paper presents a method for tracking the path and speed of meteoroids using radio observations. A simple continuous wave signal is reflected by the electrons created when the meteoroid enters the upper atmosphere and creates ionization. The reflected signal, called a meteor echo, is recorded at various locations not co-located with the transmitter. The time delays between several echoes is used to retrieve the meteoroid trajectory and speed. In this work, we apply this method using data from Belgian RAdio Meteor Stations (BRAMS), a Belgian network of 44 receiving stations. The results are compared to accurate observations from Cameras for Allsky Meteor Surveillance, an optical network of cameras surveying the sky for meteors. Our method perfectly works with no measurement errors but small uncertainties on the time delays may significantly impact the accuracy of the reconstruction. Using a large amount of receivers and/or a radio interferometer greatly improves the results. This project is the first to tackle the meteoroid trajectory reconstruction using this type of radio system (with no range information and many receivers at different locations). This novel method is essential to fully exploit the capabilities of BRAMS for future applications such as determination of fluxes or sounding of the upper atmosphere (e.g., wind speed measurements).

1. Introduction

The BRAMS (Belgian RAdio Meteor Stations) network is a Belgian project using forward scatter of radio waves to detect and characterize meteoroids. It comprises a dedicated transmitter located in the South-West of Belgium and 44 receiving stations spread all over the Belgian territory and neighboring countries (see Figure 1 for status in February 2023).

The transmitter emits a circularly polarized continuous radio wave with no modulation at a frequency of 49.97 MHz with a power of 130 W. All the receiving stations are using a 3-element Yagi antenna set up vertically and oriented in azimuth toward the transmitter. At the time of writing, approximately a third of the receiving stations is using analog ICOM-R75 receivers, an external sound card to sample the signal coming from the antenna, and is controlled by the freeware program Spectrum Lab running on a PC (Lamy et al., 2015). The other two thirds use digital SDR-RSP2 receivers controlled by a Linux system running on a Raspberry Pi (Anciaux et al., 2020). All stations are equipped with a Garmin GPS that provides timestamps to the BRAMS data and
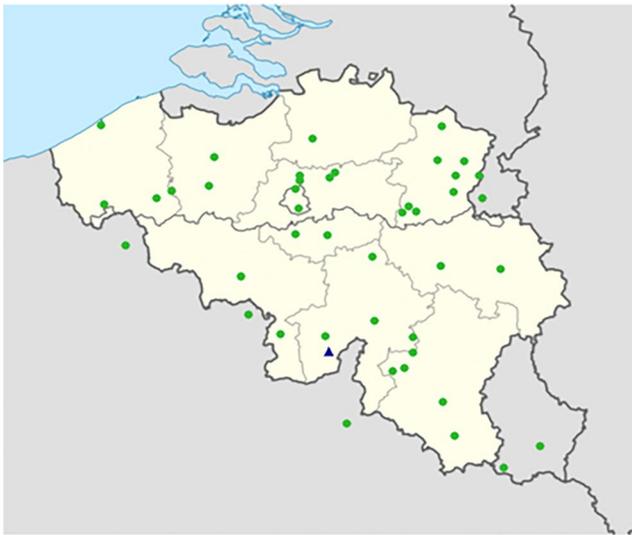
Figure 1. Map of the BRAMS network in February 2023. The blue triangle is the transmitter located in Dourbes while the green dots are the 44 active receiving stations at the time.

allows time synchronization between the receiving stations. Additional features of the receiving stations are not described here. Instead, we refer the reader to previous publications (Anciaux et al., 2020; Lamy et al., 2015).

There exist other meteor forward scatter systems but they are either associated with meteor radars (sending pulses), or continuous wave (CW) emitting systems with additional coding (e.g., phase coding). An application of such forward scatter systems is wind speed measurements in the mesosphere/lower-thermosphere (MLT) region, which have seen important developments in the last few years. Stober and Chau (2015) used data from the MMARIA (Multistatic/Multifrequency Agile Radar for Investigations of the Atmosphere) concept, made of two meteor radars and another receiver providing an additional forward scatter capability. They showed that the forward scatter observations increased both the number of meteor detections and the altitudinal coverage. Vierinen et al. (2016) introduced the concept of coded CW meteor radars and presented their advantages with respect to pulsed specular meteor radars (SMR). Notably based on this work, the MMARIA concept was further developed into SIMONe (Spread-spectrum Interferometric multistatic Meteor radar Observing Network) to extend the capabilities of traditional meteor radar systems by adding either several spatially separated receivers to existing transmitting stations, or several spatially separated transmitters to existing interferometric receiving stations (Chau et al., 2019). One unique feature of this work is the use of interferometric transmitting arrays as opposed to interferometric receiving arrays typical in meteor radars. Another example application is the measurement of ozone concentration in the MLT region, which has been indirectly performed by the Bologna-Lecce-Modra forward scatter meteor radar, thanks to the detection of meteoroids entering the Earth's upper atmosphere (Cevolani & Pupillo, 2009).

To the authors' knowledge, no existing CW forward scatter system without modulation has tackled the problem of reconstructing individual meteoroid trajectories and speeds. One of the main difficulties stems from the geometry, which is more complex than in the case of backscatter systems. For instance, as BRAMS does not modulate its CW transmitted signal, the total range traveled by the radio wave between the transmitter (Tx), the reflection point and the receiver (Rx) cannot be estimated. Therefore, the trajectory reconstruction problem is complicated to solve.

In this paper, we present an approach to retrieve meteoroid trajectories with a forward scatter CW set-up such as BRAMS. Two methods are considered: one based only on measurements of time delays between meteor echoes recorded at different receiving stations, and one using the same data but complemented with information from the radio interferometer located in the Humain station which provides the direction of one specular reflection point. In order to assess the quality of the reconstruction, a comparison with data from the optical CAMS-BeNeLux network is provided (Roggemans et al., 2016).

2. Mathematical Model

The first method (hereafter called Method 1) is based solely on geometrical considerations and relies on the specular condition of the reflection of the radio wave. The specular reflection point is the location along the meteoroid path for which the total distance traveled by the radio wave $S_i = R_{Ti} + R_{Ri}$ is minimum. In this expression, R_{Ti} is the distance from the transmitter to the meteor and R_{Ri} is the distance from the meteor to the receiver. The condition of specular reflection allows the position of the reflection point to be identified as the point on the ellipsoid, whose foci are the transmitter and the receiver, which is tangent to the meteor path. Because the geometry $Tx - Rx_i$ is different for each receiving station Rx_i, the corresponding reflection points will be located at various positions along the meteoroid path. This is illustrated in Figure 2 for a reference station Rx_0 and another station Rx_i. In this example, the specular reflection point P_0 for the reference station is created before the corresponding reflection point P_i. The distance between the two points depends on the speed V of the meteoroid. As a consequence, the reference station will detect a meteor echo shortly before receiving station i, the time delay Δt_i between meteor echoes depending on the meteoroid path and speed.
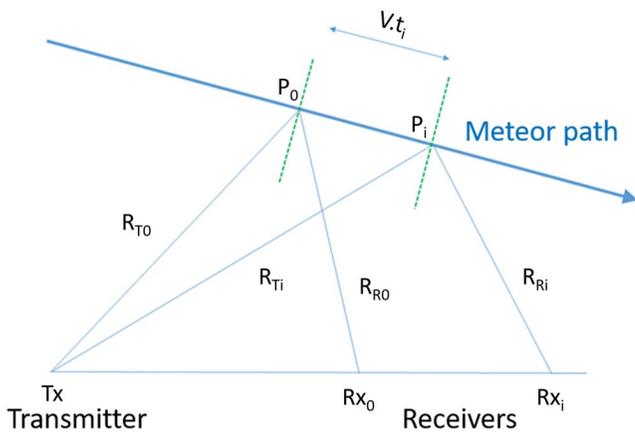
Figure 2. Specularity and geometry of a forward scatter set-up. The time delay between the creation of the specular point P_0 of the reference station Rx_0 and the specular point P_i of the other station Rx_i is noted t_i. The straight blue arrow indicates the meteor path, traveling at a speed V. The two radio wave paths $Tx - P_0 - Rx_0$ and $Tx - P_i - Rx_i$ are not coplanar.

Throughout this work, we assume that the trajectory of the meteoroid body can be described by an uniform rectilinear motion. The rectilinear assumption can be justified by the fact that the influence of the gravitational acceleration and the Coriolis forces is small compared to the magnitude of the meteor velocity: the maximum radius of curvature induced by these accelerations is respectively 2 and 12 times the radius of the Earth (Jeanne, 2020). Atmospheric drag and mass-loss can introduce significant deceleration (Kastinen & Kero, 2022; Schult et al., 2017), even for the small meteoroids detected by BRAMS. However, it is reasonable to assume that the majority of the deceleration occurs at the end of the ablation process. As most of the exploitable echoes come from the beginning and middle of the meteor event, the time delays are thus measured in a region where the constant speed assumption is acceptable.

2.1. Forward Problem

Before developing a method for retrieving the trajectory from the time delays observed at the receivers, let us study the forward problem, that is, determine the location of the specular points for a given meteor trajectory. This problem comes down to finding the intersection between an ellipsoid and a straight line (Nedeljković, 2006). If the start point is $P_1 = (x_1; y_1; z_1)$ and the end point is $P_2 = (x_2; y_2; z_2)$, the equations of the meteor trajectory are given by:

$$\frac{x - x_1}{x_1 - x_2} = \frac{y - y_1}{y_1 - y_2} = \frac{z - z_1}{z_1 - z_2}. \tag{1}$$

The description of the sought-for ellipsoid is much more complex but, given a coordinate system in which the Cartesian axes are also those of the ellipsoid, it can be described by:

$$\frac{x^2}{a^2} + \frac{y^2}{b^2} + \frac{z^2}{c^2} = 1, \tag{2}$$

where a, b, and c are real positive numbers. To facilitate use of this property, a new system of coordinates is introduced whose origin is located at the geometric center point $P_{TR} = (x_{TR}; y_{TR}; z_{TR})$ between the transmitter and the receiver. We define the y-axis in the same direction as the vector joining these points. The considered ellipsoid is a spheroid (i.e., an ellipsoid of revolution) because the two ranges $R_{Ti} + R_{Ri}$ are fixed but the location of the reflection point is arbitrary. As a result, we deduce $a = c$, such that Equation 2 can be expressed as:

$$\frac{x^2}{a^2} + \frac{y^2}{b^2} + \frac{z^2}{a^2} = 1. \tag{3}$$

This system can be obtained with the following transformations: a translation to set the location of the ellipsoid center P_{TR} as the origin of the reference frame (conversion between system 0 and ′):

$$\begin{aligned} x' &= x_0 - x_{TR}, \\ y' &= y_0 - y_{TR}, \\ z' &= z_0 - z_{TR}, \end{aligned} \tag{4}$$

a rotation around the z-axis by an angle $\alpha = \arctan\left(\frac{x_{TR}}{y_{TR}}\right)$ (angle between system ′ and ″):

$$\begin{aligned} x'' &= \cos(\alpha)x' - \sin(\alpha)y', \\ y'' &= \sin(\alpha)x' + \cos(\alpha)y', \\ z'' &= z', \end{aligned} \tag{5}$$

and a rotation around the x-axis by an angle $\beta = -\arctan\left(\frac{z_{TR}}{y_{TR}}\right)$ (angle between system $''$ and $'''$):

$$x''' = x'',$$
$$y''' = \cos(\beta)y'' - \sin(\beta)z'', \tag{6}$$
$$z''' = \sin(\beta)y'' + \cos(\beta)z''.$$

This last reference frame is the one in which the determination of the specular point location is performed. In the following, we will drop the superscript $''$ for clarity. Thus, x, y, z should be understood as x''', y''' and z''' for the rest of this subsection.

Using Equation 1, we can deduce x and z values from y and obtain the following system of equations:

$$x = \frac{x_1 - x_2}{y_1 - y_2}(y - y_1) + x_1,$$
$$z = \frac{z_1 - z_2}{y_1 - y_2}(y - y_1) + z_1. \tag{7}$$

Using these values in Equation 3, we obtain a quadratic equation of the form $Ay^2 + By + C = 0$, whose solutions are given by:

$$y_{1,2} = \frac{-B \pm \sqrt{B^2 - 4AC}}{2A}. \tag{8}$$

Because we are looking for a tangent point, we already know that there the solution is unique, which means that:

$$B^2 - 4AC = 0, \tag{9}$$

where A, B, and C are functions of a, b, P_1, and P_2. Replacing a^2 by $b^2 - f^2$ (where f is half the interfocal distance of the ellipsoid), this gives us a fourth order equation in b. This equation can be solved for b^2 and then for $a^2 = b^2 - f^2$ with a and b being chosen so that they are positive values. Knowing a and b, we are able to compute A, B, and then y. From Equation 7, we find the full position vector $P_{\text{Tan}} = (x; y; z)$ in the system $''$.

The final step is to perform an inverse transformation to come back to an easy-to-use and more general coordinate system (i.e., not linked to a specific ellipsoid). It is natural to choose Dourbes, where the BRAMS transmitter Tx is located, as the origin of this global reference system. Like in previous work on the BRAMS network (Lamy & Tétard, 2016), the West-East direction is used as the X-axis and the South-North direction as the Y-axis. The Z-axis is taken out of the plane by the right-hand rule. This reference frame is used for our following computations.

2.2. Inverse Problem

We have defined a way to compute the location of the specular points, knowing the meteoroid trajectory. In practice however, the trajectory is unknown. To find it, the only inputs at our disposal with Method 1 are the time delays between meteor echoes observed at the receiving stations. The trajectory reconstruction problem is thus inverse.

More formally, a meteoroid trajectory can be defined by the 3D Cartesian coordinates of one specular point (the one corresponding to a reference station) and the three components the velocity which provide the direction (assuming again a constant speed). This gives a total of six unknowns (respectively called X_0, Y_0, Z_0, V_x, V_y, and V_z) and therefore the need to have at least six equations to avoid solving an underdetermined system. In Method 1, these equations are provided by the specularity condition. Let us write the distance S_i, traveled by the radio wave from the transmitter toward a reflection point $P_i = (X_i, Y_i, Z_i)$ and back to the receiver $Rx_i = (x_i, y_i, z_i)$:

$$S_i = \sqrt{X_i^2 + Y_i^2 + Z_i^2} + \sqrt{(X_i - x_i)^2 + (Y_i - y_i)^2 + (Z_i - z_i)^2}, \tag{10}$$

where, for each receiver Rx_i:

$$\begin{pmatrix} X_i \\ Y_i \\ Z_i \end{pmatrix} = \begin{pmatrix} X_0 \\ Y_0 \\ Z_0 \end{pmatrix} + \Delta t_i \begin{pmatrix} V_x \\ V_y \\ V_z \end{pmatrix}, \tag{11}$$

which formalizes the fact that there is a time delay Δt_i between the creation of the specular point P_i of the receiver Rx_i and the specular point P_0 of the receiver Rx_0 (see Figure 2). The specularity condition implies that the total distance traveled by the radio wave is minimum at the specular reflection point, hence $\frac{dS_i}{dt} = 0$. This time derivative can be expressed as:

$$\frac{dS_i}{dt} = \frac{\partial S_i}{\partial X_i}\frac{dX_i}{dt} + \frac{\partial S_i}{\partial Y_i}\frac{dY_i}{dt} + \frac{\partial S_i}{\partial Z_i}\frac{dZ_i}{dt}. \tag{12}$$

The partial derivatives with respect to the specular point coordinates can be obtained through (example given for X_i, the same principle can be applied for Y_i and Z_i):

$$\frac{\partial S_i}{\partial X_i} = \frac{X_i}{\sqrt{X_i^2 + Y_i^2 + Z_i^2}} + \frac{X_i - x_i}{\sqrt{(X_i - x_i)^2 + (Y_i - y_i)^2 + (Z_i - z_i)^2}}. \tag{13}$$

Using the assumption of constant speed motion, we have $\frac{dX_i}{dt} = V_x$, $\frac{dY_i}{dt} = V_y$ and $\frac{dZ_i}{dt} = V_z$. Combining Equations 12 and 13 and using the fact that S_i should be minimum at each receiving station, we obtain:

$$\begin{aligned}\frac{dS_i}{dt} &= \frac{X_i \cdot V_x + Y_i \cdot V_y + Z_i \cdot V_z}{\sqrt{X_i^2 + Y_i^2 + Z_i^2}} \\ &+ \frac{(X_i - x_i) \cdot V_x + (Y_i - y_i) \cdot V_y + (Z_i - z_i) \cdot V_z}{\sqrt{(X_i - x_i)^2 + (Y_i - y_i)^2 + (Z_i - z_i)^2}} \\ &= 0.\end{aligned} \tag{14}$$

As X_i, Y_i, and Z_i depend on the input time delay Δt_i through Equation 11, we have an implicit link between the input of our system and the output trajectory, described by our six parameters. This set of equations is highly nonlinear and is therefore particularly difficult to solve.

A nonlinear solver that takes into account additional constraints on the unknowns is then used. On the one hand, the height of all reflection points must lie between for example, 80 and 120 km altitude. Above this interval, the atmospheric density is too low for the radio signals to be reflected by the ionized trail. Below it, the low-mass meteoroids that we are interested in are completely disintegrated into dust. On the other hand, the speed of most meteoroids is larger than ~11 km/s but smaller than ~72 km/s. The lower limit corresponds to the Earth's escape velocity, while the upper limit is the maximum geocentric speed at which a Solar System object can enter the Earth's atmosphere. Meteoroids of interstellar origin may pass through our atmosphere with a speed of more than 72 km/s, but these cases are very rare (Froncisz et al., 2020; Hajduková Jr. et al., 2014).

The second method (hereafter called Method 2) is using the same assumptions as Method 1 but includes data from our interferometric radio station located in Humain. Unlike the other receiving stations, it uses 5 antennas in the so-called Jones configuration (Jones et al., 1998; Lamy et al., 2018) and allows to determine the direction of arrival of the meteor echo to within approximately 1°, although errors on azimuth and elevation have different dependencies (Jacobs & Ralston, 1981). The interferometer provides two more equations for the azimuth and elevation of the specular reflection point but does not provide its exact position. With these additional equations, we theoretically need time delays measured between only 3 additional stations and a reference station in order to get at least 6 equations.

3. Solver Development

The nonlinear optimization solver that we will use is based on an interior-point (IP) method (Karmarkar & Ramakrishnan, 1991). The IP algorithms are used in solving both linear and nonlinear convex optimization problems that contain inequalities as constraints. In our case, these inequality constraints are related to the altitude of the reflection points and the meteoroid speed. There are two important IP algorithms: the barrier approach and the primal-dual method. The primal-dual approach is preferred here due to its efficiency and accuracy. Further information about the IP approach can be found in Boyd and Vandenberghe (2004).

3.1. Target Definition

The most important quantity to define is the target objective (or cost function) to minimize. This function associates a scalar to every trajectory (defined by our 6 unknowns): the lower its value, the better the reconstruction (given the input time delays that we have at our disposal).

For Method 1, the first dimensionless target objective that we defined comes from the specularity condition:

$$J_0 = \frac{1}{n} \sum_{i=1}^{n} \left(\frac{dS_i}{dt} \cdot \frac{1}{V} \right)^2,$$

(15)

where $V = \sqrt{V_x^2 + V_y^2 + V_z^2}$ is used to make the target objective dimensionless, and the sum is done on n receivers. This approach is the most intuitive as it uses the minimization of the distance traveled by the radio wave. Nonetheless, it shows two major drawbacks. First, it is very sensitive to the quality of the initial guess. Indeed, as the IP approach is gradient-based, we need to prescribe a first solution to the solver. We observed that this guess needs to be quite close to the correct solution to ensure solver convergence, which is problematic given we generally have no a priori knowledge of the trajectory.

The second drawback is that this target does not explicitly use the measured time delays at our receivers. However, the idea of comparing the measured physical quantities to forward modeled ones through use of their uncertainty distributions is powerful, as it allows the construction of a Bayesian inference approach to model parameter estimation. This approach tends to be robust as it includes the errors at their source, utilizes maximal information (no information is lost through further processing), quickly reveals model limitation to fitting the data, and allows for explicit evaluation of how well the model parameters can be determined for each case (Kastinen & Kero, 2022; Markkanen et al., 2005).

To alleviate these drawbacks, we introduce another target objective for Method 1, defined as:

$$J_1 = \sum_{i=1}^{n} w_i \left(\frac{\Delta t_{i,model} - \Delta t_{i,obs}}{\max_i \left(|\Delta t_{i,obs}| \right)} \right)^2,$$

(16)

where $\Delta t_{i,obs}$ is the experimental time delay measured at a receiver, while $\Delta t_{i,model}$ is a theoretical time delay coming from the forward problem described in Section 2.1. Indeed, given a trajectory, we can run the forward problem, compute the time delays that we should observe theoretically at the receivers and compare them with our measurements. By minimizing the difference between $\Delta t_{i,obs}$ and $\Delta t_{i,model}$ at each receiver, we are actually finding the trajectory which gives the smallest difference between observed time delays and modeled ones, that is, the "best" trajectory given our set of inputs.

Depending on the geometry as well as on the characteristics of the receiving stations, some echoes will be stronger while others will be fainter. To account for these differences, we introduce a weight w_i, which captures the uncertainty that we have on the measured time delays. In our case, we weigh each time delay by the signal-to-noise ratio (SNR) obtained at the receiver, that is, as the echo is stronger, we assume that the time delay measurement will be more reliable.

For Method 2, we use the following target objective:

$$J_2 = J_1 + \left(\frac{\varepsilon - \operatorname{atan}\left(\frac{Z_H - z_H}{\sqrt{(X_H - x_H)^2 + (Y_H - y_H)^2}} \right)}{\delta \varepsilon} \right)^2 + \left(\frac{\theta - \operatorname{atan}\left(\frac{Y_H - y_H}{X_H - x_H} \right)}{\delta \theta} \right)^2,$$

(17)

where J_1 is computed from Equation 16, ε and θ are respectively the elevation and azimuth angle coming from the interferometer, which are computed as described in Jones et al. (1998). $P_H = (X_H; Y_H; Z_H)$ are the coordinates of Humain specular point and $R_H = (x_H; y_H; z_H)$ are the coordinates of the receiver in Humain. $\delta \varepsilon$ and $\delta \theta$ are the uncertainties associated to the interferometric data.

3.2. Solver Validation

To validate the trajectory reconstruction solver, 10 synthetic trajectories are simulated. They are drawn from optical data given by the CAMS-BeNeLux network (Jenniskens et al., 2011; Roggemans et al., 2016). Data were provided for 2 clear consecutive nights from 29 to 31 July 2020, in a period without any strong activity from meteor showers. At this date, the BRAMS network had only 28 active receivers. Among the 948 available

Table 1
CAMS Trajectories for the Solver Validation

No.	X_H (km)	Y_H (km)	Z_H (km)	V_x (km/s)	V_y (km/s)	V_z (km/s)
79	44.33	59.11	94.90	−24.59	31.22	−12.70
105	121.59	95.16	99.39	−18.98	34.62	−12.95
188	−52.88	23.12	88.13	0.55	29.19	−5.70
282	−96.09	35.92	88.28	−2.86	36.80	−16.88
477	−77.35	11.34	104.90	−35.37	−39.62	−30.68
532	38.67	51.64	91.67	−26.51	31.40	−11.89
536	21.62	199.76	105.64	−58.06	13.41	−26.14
598	6.18	158.68	103.13	−70.09	−4.60	−5.27
709	−32.21	108.29	97.79	−37.75	23.15	−45.79
773	−92.91	61.60	98.18	−37.61	14.15	−52.09

Note. No. indicates the trajectory identification number from the CAMS data. X_H, Y_H, and Z_H are the coordinates of the specular reflection point for the Humain station in a Cartesian referential centered on the Dourbes transmitter. X is directed East-West and counted positive toward East, Y is directed North-South and counted positive toward North. V_x, V_y, and V_z are the velocity components of the meteoroid determined by CAMS and projected in this reference frame.

trajectories, most of them are not located above Belgium and therefore not geometrically suitable to be detected by our BRAMS receiving stations. A selection was made based on the following criteria: (a) each trajectory must be detected by at least 6 stations, (b) because we want to compare Methods 1 & 2, one of these stations must be the interferometer in Humain, and (c) we restrict ourselves as much as possible to underdense meteor echoes in order to ensure that the specularity condition is valid. The application of these criteria resulted in a selection of 10 suitable CAMS trajectories. The parameters of these trajectories are summarized in Table 1.

The idea behind those simulated trajectories is to verify the proper functioning of the solver when there are no measurement errors, that is, checking that we recover the targeted trajectory assuming we have a perfect knowledge of the time delays at the receivers. To do so, the known CAMS trajectory is used to get the theoretical time delays, through the forward problem described in Section 2.1. The latter are then fed inside the inverse solver, and the output trajectory is compared with the CAMS one.

As shown in Figure 3, the errors are of the same order of magnitude on the 10 reconstructed trajectories: about 0.001° on the inclination angle, a few meters on the reflection point location and about 1 m/s on the velocity. This analysis demonstrates the proper functioning of our solver as it yields the correct solution if the inputs are free of measurement errors.

3.3. Uncertainty Quantification

As discussed for the Canadian Meteor Orbit Radar (CMOR) network by Mazur et al. (2020), the inverse trajectory reconstruction problem is severely ill-conditioned when no interferometric information is used, all the receiving stations lie close to each other (less than 20 km between two receivers) and are almost on the same plane. The latter is true since the differences in altitude between the receivers are only of a few tens of meters while the trajectories are located at about 100 km in altitude. In this configuration, the output trajectories are highly sensitive to the quality of the input time delays, small errors on the latter leading to large uncertainties on the trajectory parameters.

To verify if this statement holds true with our forward scatter CW problem, we perform a Monte-Carlo uncertainty quantification campaign. For each simulated trajectory, it consists in building a Gaussian distribution of
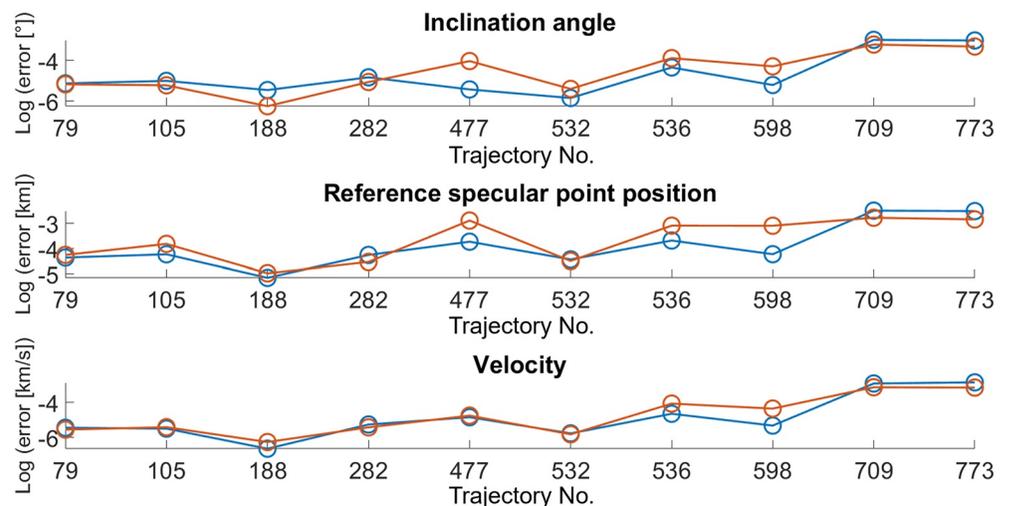
Figure 3. Reconstruction errors in logarithmic scale for 10 synthetic trajectories with Method 1 (in blue) and Method 2 (in red). Top panel: error on the inclination angle. Middle panel: error on the reference specular point position. Bottom panel: error on the velocity.
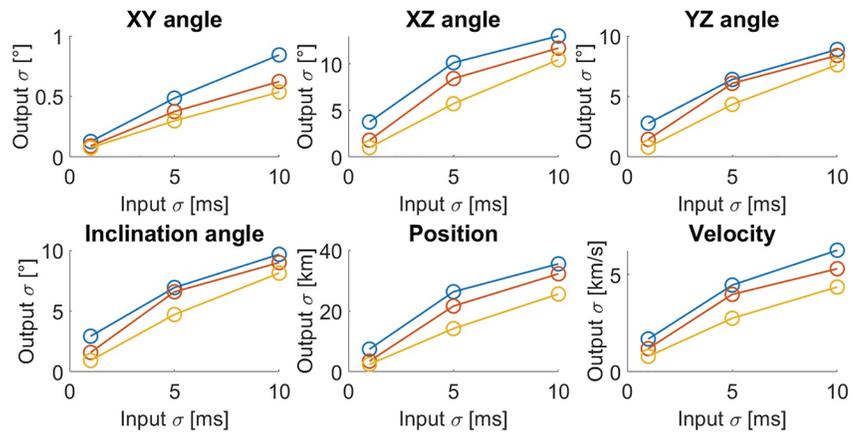
Figure 4. Uncertainty quantification results for Method 1 with 6 stations (in blue), 9 stations (in red), 12 stations (in yellow). Top panel: uncertainties on the trajectory angles (in the *XY* plane on the left, *XZ* plane in the middle, *YZ* plane on the right). Bottom panel: uncertainties on the inclination angle (on the left), reference specular point position (in the middle) and velocity (on the right).

time delays at a chosen number of BRAMS receivers (6, 9, or 12 stations), centered on the theoretical time delay (which is calculated for the 10 CAMS trajectories with the forward problem). Three values of standard deviation σ of these Gaussian distributions are studied: 1, 5, and 10 ms.

For each of these values, and for each of the 10 simulated trajectories, we draw 1,000 sets of time delays. Then, each of these sets is fed inside our solver, and a corresponding output trajectory is computed, with the target objective given in Equation 16. We can then gather the output solutions into distributions and check their standard deviation. The uncertainty quantification results obtained with Method 1 are shown in Figure 4.

Two main observations can be made: first, it appears that only the angle in the horizontal plane *XY* is retrieved with an uncertainty of less than 1°. In the vertical directions, uncertainties of about 5 ms on the input time delays already lead to inclination errors of about 5–10°. The same observation holds for the reconstruction of the specular point position and of the velocity. This illustrates the ill-conditioning of the trajectory reconstruction problem without interferometry. Another important observation is that, as the number of stations that are used for the reconstruction increases from 6 to 12, the sensitivity of the output trajectory with respect to the input time delays is decreased. This shows the benefit of having more than 6 receivers detecting the signals, as errors in the determination of the time delays at different receivers can then compensate each other.

The results of the uncertainty quantification campaign run with Method 2 are shown in Figure 5. The target objective used for these trajectory reconstructions is given by Equation 17. In this case, the uncertainties on the elevation $\delta\epsilon$ and on the azimuth $\delta\theta$ of the Humain specular point are ~1°, in agreement with Jones et al. (1998, 2005). The SNRs of the considered meteor events are high since they were also detected by cameras. However, it should be noted that the 1° accuracy deteriorates at low SNR.

As already observed for CMOR by Mazur et al. (2020), the use of the interferometer alleviates the ill-conditioning of the trajectory reconstruction problem. Indeed, it appears that the uncertainties on the inclination, on the reference specular point position and on the velocity are decreased by about an order of magnitude. As an illustration, the inclination angle with about 10 ms of uncertainty on the time delays is known within an uncertainty of less that 1° with the interferometer, while it was of about 10° with Method 1. This statement holds true whatever the number of receivers taken into account for the reconstructions, further highlighting the benefits brought by interferometric data.

4. Radio Data Processing

Several methods can be used for the determination of time lags between two receivers. The first possibility is to use the cross-correlation peak between the signals coming at two receivers. This approach has however two significant drawbacks: on the one hand, since the location of the specular point will be different for both receivers,
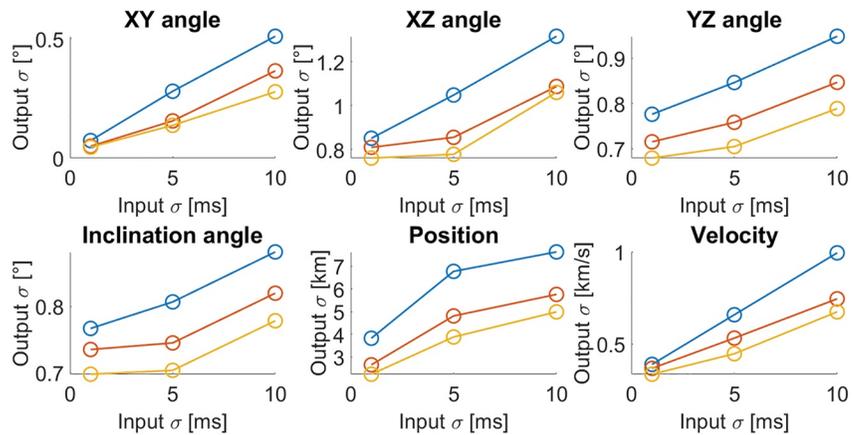
Figure 5. Uncertainty quantification results for Method 2 with 6 stations (in blue), 9 stations (in red), 12 stations (in yellow). The panels are the same as in Figure 4.

the echoes coming from two receivers can look very different. One can for instance be located at an altitude where the reflection is rather underdense, while the other would be more overdense. On the other hand, the BRAMS receiving stations have different characteristics in terms of noise levels. For echoes with a low SNR, this can lead to a difference in detection points, and thus to a large error on the identification of the cross-correlation peak timing. This problem was already observed for the Advanced Meteor Orbit Radar (AMOR) network by Baggaley et al. (1994). Instead, we prefer to use a physics-based reference point on each signal, which can then be used to compute time delays.

4.1. Cornu Spiral

To do so, it is important to remember that radio systems work well to detect reflected signals from small meteoroids. As a result of this, most of the echoes which will be of interest for us will be underdense. Thus, the received power during the formation of the trail, considering an infinite trail length and homogeneous ionization, is given by McKinley (1961) and Wislez (2006):

$$P(t) = P_0 \frac{1}{2} \left(\left[\int_{-\infty}^{x(t)} \cos \frac{\pi x^2}{2} dx \right]^2 + \left[\int_{-\infty}^{x(t)} \sin \frac{\pi x^2}{2} dx \right]^2 \right) = $$
$$P_0 \frac{1}{2} \left(\mathcal{F}_{\cos}^2 + \mathcal{F}_{\sin}^2 \right), \tag{18}$$

where $\mathcal{F}_{\cos}$ and $\mathcal{F}_{\sin}$ are the Fresnel integrals, and x is the Fresnel parameter along the spiral formed by the parametric plot of the Fresnel integrals. The exact expression of P_0 can be found in McKinley (1961).

As described by Mazur et al. (2020), a plot of $\mathcal{F}_{\sin}$ against $\mathcal{F}_{\cos}$ produces the Cornu spiral which allows for a graphical representation of the time-varying component of the echo amplitude A from:

$$A = \sqrt{(\Delta \mathcal{F}_{\cos})^2 + (\Delta \mathcal{F}_{\sin})^2}, \tag{19}$$

where $\Delta \mathcal{F}_{\cos}$ and $\Delta \mathcal{F}_{\sin}$ are distances in the parametric plot from the starting point $(-0.5; -0.5)$. The Cornu spiral as well as the variations of echo amplitude A are shown in Figure 6. The specular point is identified as the point $(0; 0)$ on the Cornu spiral (see top panel) and corresponds to $x = 0$. Looking at the bottom panel, the dimensionless amplitude at the specular point is 0.427.

In practice, we will never observe a smooth amplitude curve as the one shown in Figure 6. Indeed, the raw signal at the time of the meteor echo is always noisy and very often has other superimposed signals on it, such as the direct signal coming from the beacon or interfering aircraft. These affect the meteor signal by adding a spectral component and modifying its amplitude and phase. They can also cause an interference beat if they have slightly different frequencies. Therefore, a pre-processing of the data is necessary to properly exploit the echoes of the
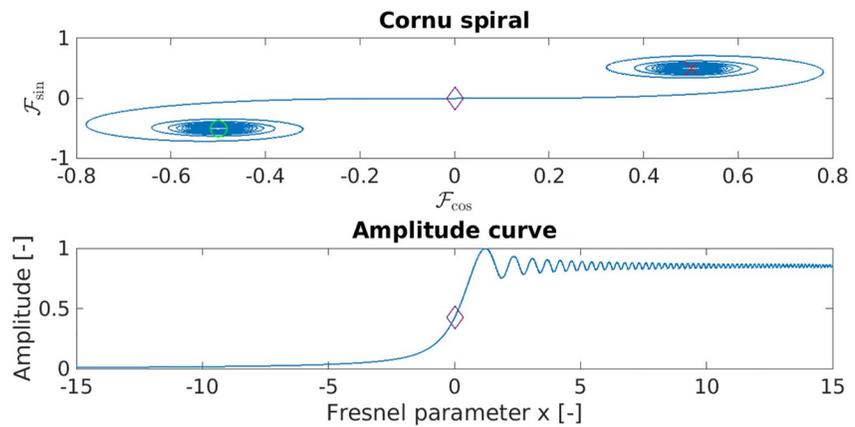
Figure 6. Cornu spiral and corresponding amplitude curve. Top panel: the spiral and its characteristic points. The green circle indicates the start of the spiral (in $x = -\infty$), the purple diamond is the passage at the specular point ($x = 0$), and the red cross is the end of the spiral (in $x = +\infty$). Bottom panel: Amplitude variation with the Fresnel parameter x. The specular point is highlighted with a purple diamond.

detected meteors. The two following sections describe the methods used to subtract the beacon signal and to filter out the noise.

4.2. Beacon Signal Subtraction

The basic principle behind the method used to remove the beacon signal is to reconstruct and then subtract it from the full signal. As mentioned above, the transmitter emits a pure cosinusoidal wave, whose amplitude and phase vary at each receiver. The received beacon signal is:

$$b(t) = A\cos(2\pi f_0 t + \phi), \tag{20}$$

where $b(t)$ is the temporal signal, A its amplitude, f_0 its frequency and ϕ its phase. However, the lack of stability of the local oscillator of the first BRAMS stations (due to temperature variations in the analog receiver) as well as distortions (due to tropospheric propagation) can affect the initial signal and change the amplitude, frequency and phase parameters.

The subtraction method that we developed is based on the analysis of the Fourier transform of the signal around the beacon frequency. Since the beacon signal is a pure cosinusoidal wave, its Fourier transform is given by:

$$B(f) = \frac{1}{2}\left[\delta(f - f_0)e^{i\phi} + \delta(f + f_0)e^{-i\phi}\right], \tag{21}$$

which has Hermitian-symmetry with respect to frequency. The real-valued received signal is measured over a finite number of samples and its discrete Fourier transform (DFT) is computed using the Fast Fourier Transform algorithm (FFT). Because of the inherent symmetry of the spectrum, only positive frequencies need be considered; the negative-frequency terms are redundant. Moreover, the DFT is computed over a finite-time interval, which corresponds to a multiplication of the raw signal by a rectangular time window whose DFT is a sinc function (J. O. Smith, 2011):

$$W_r(f) = A\tau\text{sinc}(\tau f) = A\frac{\sin(\pi\tau f)}{\pi f}, \tag{22}$$

where τ is the duration of the finite-time interval.

Thus, the DFT of the meteor signal over a finite-time interval is the DFT of the product between the raw signal and a time window, which means the convolution product between a Dirac delta function δ and a sinc function in the spectral domain. This convolution gives a sinc function centered on the δ position. The sinc is thus centered on the received beacon frequency and has an amplitude equal to that of the received beacon signal. But because the DFT only samples the underlying Fourier transform at multiples of the sampling frequency, its maximum
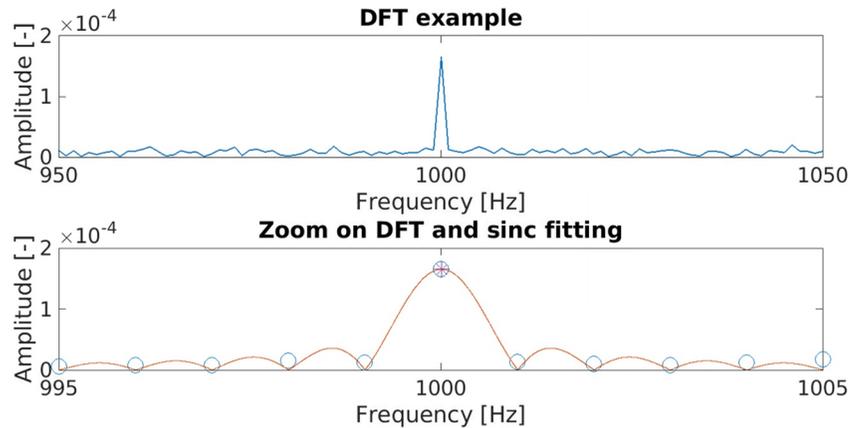
Figure 7. Example of a DFT on a 1 s interval and corresponding sinc fitting. Top panel: DFT on the whole frequency spectrum. Bottom panel: zoom around the beacon frequency and sinc function fitting. The blue circles are the DFT samples, the red curve is the sinc function fitted on these points and the purple star is the maximum of the fit.

does not necessarily coincide with the maximum of the sinc function. It is thus necessary to fit a sinc to the DFT points in order to retrieve the amplitude A and frequency f of the peak. This procedure is illustrated in Figure 7.

In order to compute the phase ϕ, the following formula is used:

$$\phi = \phi_0 + \delta\pi\frac{N-1}{N} - 2\pi f_b t_s, \tag{23}$$

where ϕ_0 is the phase at the maximum of the discrete FFT, N is the number of points on which the FFT is computed, and f_b is the beacon frequency obtained with the fit of the sinc function. The second term is a correction to get the phase at the maximum of the continuous fitted sinc, where δ is the difference of frequency index between the discrete peak of the FFT and its continuous peak. The last term is a linear time correction where t_s represents the timing at which the considered time interval starts.

In order to maximize the frequency resolution, the whole time interval of 300 s contained in each radio file should ideally be used to compute the FFT. However, the longer this time interval, the more likely the signal is subject to small variations of the local oscillator and/or variation of tropospheric conditions. A balance has thus to be found between instabilities and frequency resolution. Experience has shown that, in practice, short time intervals give better results even if the frequency resolution is decreased. Therefore, we decide to split each radio file in small intervals of 1 s in which the reconstruction is done independently.

Two further remarks need to be made. First, to reduce the spectral leakage characteristic of the rectangular window, we decide to use a Hann window (Harris, 1978; Nuttall, 1981) so that the function fitted in the frequency domain is:

$$W_h(f) = \frac{A}{2}\frac{\mathrm{sinc}(\tau f)}{(1-\tau^2 f^2)}. \tag{24}$$

Second, this whole approach works fine as long as there is no other signal superimposed on the beacon frequency, such as a meteor. To account for this possibility, we use a statistical criterion looking at the Hann window fit quality on each consecutive 1 s interval. If the fit on a given interval is more than 3 median absolute deviation (MAD) worse than the median fit quality over 300 s, the reconstruction in this interval is rejected. In this case, the amplitude, frequency and phase are interpolated from the neighboring intervals. The results obtained with this approach are displayed in Figure 8. While it appears that the subtraction without interpolation (middle panel) introduces some spectral artifact for the meteor highlighted in the red rectangles, the approach with interpolation (bottom panel) preserves its shape.

4.3. Filtering and Smoothing

After the beacon signal has been subtracted, the noise has to be filtered to isolate the actual echo coming from the meteor. To do this, we use a windowed-sinc band-pass filter defined by the product of a sinc function and a Blackman window. This approach significantly reduces the noise level while keeping a steep transition band and an excellent stopband attenuation, as described in S. Smith (2013).
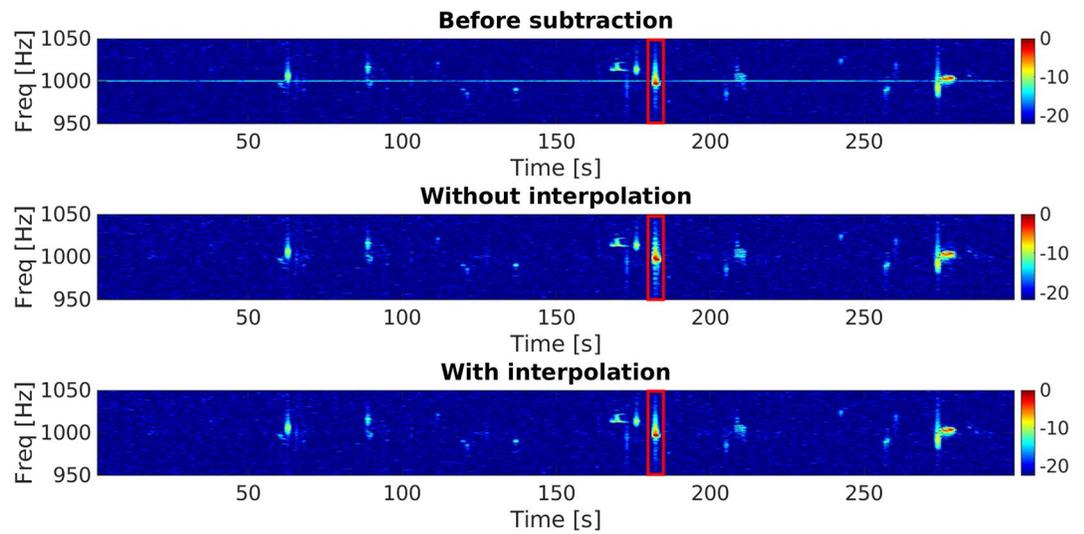
Figure 8. Example of spectrograms before and after beacon signal subtraction. Top panel: Raw spectrogram before processing. Middle panel: Spectrogram after beacon subtraction without interpolation. Bottom panel: Spectrogram after beacon subtraction with interpolation. In the three panels, the power is color-coded in dB FS (Decibels relative to Full Scale). The red rectangles highlight the same meteor in the three spectrograms.

The band-pass filter expression is obtained from the convolution of a low-pass filter and a high-pass filter. The design of such filters requires the selection of two parameters: the cut-off frequency f_c and the length of the filter kernel M (number of points of the truncated sinc). M can be computed using:

$$M \approx \frac{4}{BW}, \tag{25}$$

where BW is the width of the transition band in the filter frequency response (magnitude of its transfer function), measured from where the curve just barely leaves one to where it almost reaches zero. To have a good trade-off between a sharp transition band and a reasonable length of the filter kernel, BW is always chosen equal to 4×10^{-3} so that $M = 1,000$ points. After the selection of f_c and M, the filter kernel is calculated with:

$$h[i] = K \frac{\sin\left(2\pi f_c \left(i - \frac{M}{2}\right)\right)}{i - \frac{M}{2}} \left[0.42 - 0.5\cos\left(\frac{2\pi i}{M}\right) + 0.08\cos\left(\frac{4\pi i}{M}\right)\right]. \tag{26}$$

Three components can be identified: a constant K chosen to provide unity gain at the maximum of the window, the sinc function with a $\frac{M}{2}$ shift to get only positive index values and the Blackman window equation.

Most of the meteor echoes detected are located in a range of 100 Hz around the beacon frequency f_b. However, if a too narrow filter is used, the dynamics of the filtered meteor echo will be modified too strongly by the impulse response of the filter. This is illustrated in Figure 9, where the rise of the echo is made unphysically longer by a bandpass of 60 Hz. Heuristically, we find that a bandpass of 600 Hz, that is, $f_{high} = f_b - 300$ Hz and $f_{low} = f_b + 300$ Hz is a good trade-off between noise reduction and preservation of the signal dynamics.

The very good frequency performance of the windowed-sinc filter contrast with its poor characteristics in the time domain, notably in terms of ripple and overshoot in the step response. Moreover, as we filter the signal with a bandpass of 600 Hz, it sometimes happen that another parasitic signal in this frequency band remains unfiltered. As a result, oscillations with the meteor

Figure 9. Example of amplitude curves of a meteor echo for two windowed-sinc filters. The blue and red curves are respectively obtained with a filter passband of 600 and 60 Hz.
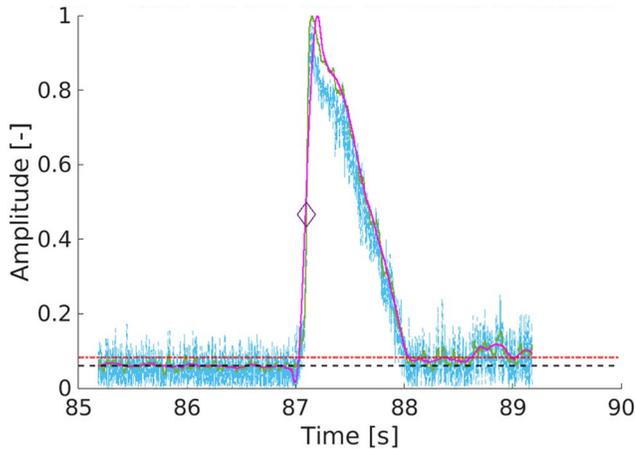
Figure 10. Example of amplitude curves of a meteor echo for two Savitzky-Golay windows. The blue curve is obtained without smoothing, while the green and magenta curves are obtained with a smoothing window of respectively 301 and 1,501 points. The purple diamond is the specular point. The dashed black line is the median noise level. The dashed-dotted red line is the median + 3 MAD level.

echo are created and deteriorate the identification of the timing corresponding to the specular point.

Therefore, a Savitzky-Golay (SG) filter is applied to the data points (Savitzky & Golay, 1964). The idea is the following: for each point in the signal, a polynomial is fitted to that point and the neighboring ones. The value of the polynomial is evaluated at that point and taken as the value of the filtered signal. The filtering operation can be reduced to the calculation of a convolution product of the signal by a kernel adapted to the user's choice: polynomial degree on the one hand, and number of neighboring points used for the filter (i.e., window length) on the other hand.

Heuristically, we choose a polynomial order of 3 and a window length of 301 points. The reason for this choice is that a too small window does not dampen the oscillations enough, while a too large one tends to oversmooth the rise of the meteor echo. The output amplitude curve obtained with two different SG filters for a chosen echo is shown in Figure 10. The specular point (corresponding to a dimensionless amplitude of 0.427) is highlighted on the amplitude curve with a window length of 301 samples. The median and median + 3 MAD noise levels are computed on an interval of 2 s before the start of the meteor echo.

The exact timing (in UTC reference) of the specular point can be identified thanks to the GPS timestamps. A further correction is applied to account for the delays of the different types of receivers. Each has its own band-pass filter with its own response time that needs to be compensated for, in order to compare the timings at several stations. The procedure to obtain these delays will be explained in a future paper describing in detail the BRAMS network.

Finally, the solver described in Section 3 is called with the time delays as inputs, and outputs a reconstructed trajectory. A summary of the complete workflow is given in Figure 11.

5. Comparison With Optical Trajectories

In this section, we compare reconstructions obtained with the BRAMS data and the optical trajectories given by the CAMS-BeNeLux network, for the 10 cases presented in Table 1. At the time of writing, the CAMS network in the Benelux consists of about 100 cameras that cover the sky above Belgium, The Netherlands, Luxembourg and part of Germany. In the case where several cameras record the same meteor, its trajectory and speed are calculated with a very good accuracy, so that we can use them as a reference. Indeed, CAMS can compute radiants with an uncertainty of less than 2° and speeds with an uncertainty of less than 10% (Jenniskens et al., 2016). Further information about the network can be found in Roggemans et al. (2016).

For each trajectory, the CAMS data file contains the following parameters:

- The time interval during which the meteor was visible by certain cameras.
- The geographical position (longitude, latitude and altitude) of the start and end points of the visible trajectory.
- The total velocity V_∞ corresponding to the appearance of the meteor (associated entry into the atmosphere).
- The acceleration parameters a_1 and a_2 modeled by CAMS (Jacchia et al., 1967).
- The uncertainties (standard deviation) on the positions, velocity and acceleration parameters.

CAMS use a deceleration model introduced by Whipple and Jacchia (1957) and Jacchia et al. (1967):

$$V(t) = V_\infty - |a_1 a_2| \exp(a_2 t), \qquad (27)$$

where $t = 0$ corresponds to the timing of the first recorded trail. Since we use a constant speed assumption in our reconstruction method, the comparison between our velocity output and the velocity given by CAMS is not
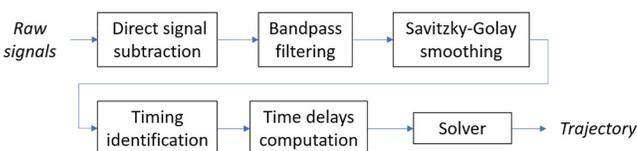
Figure 11. Workflow for the trajectory reconstruction.
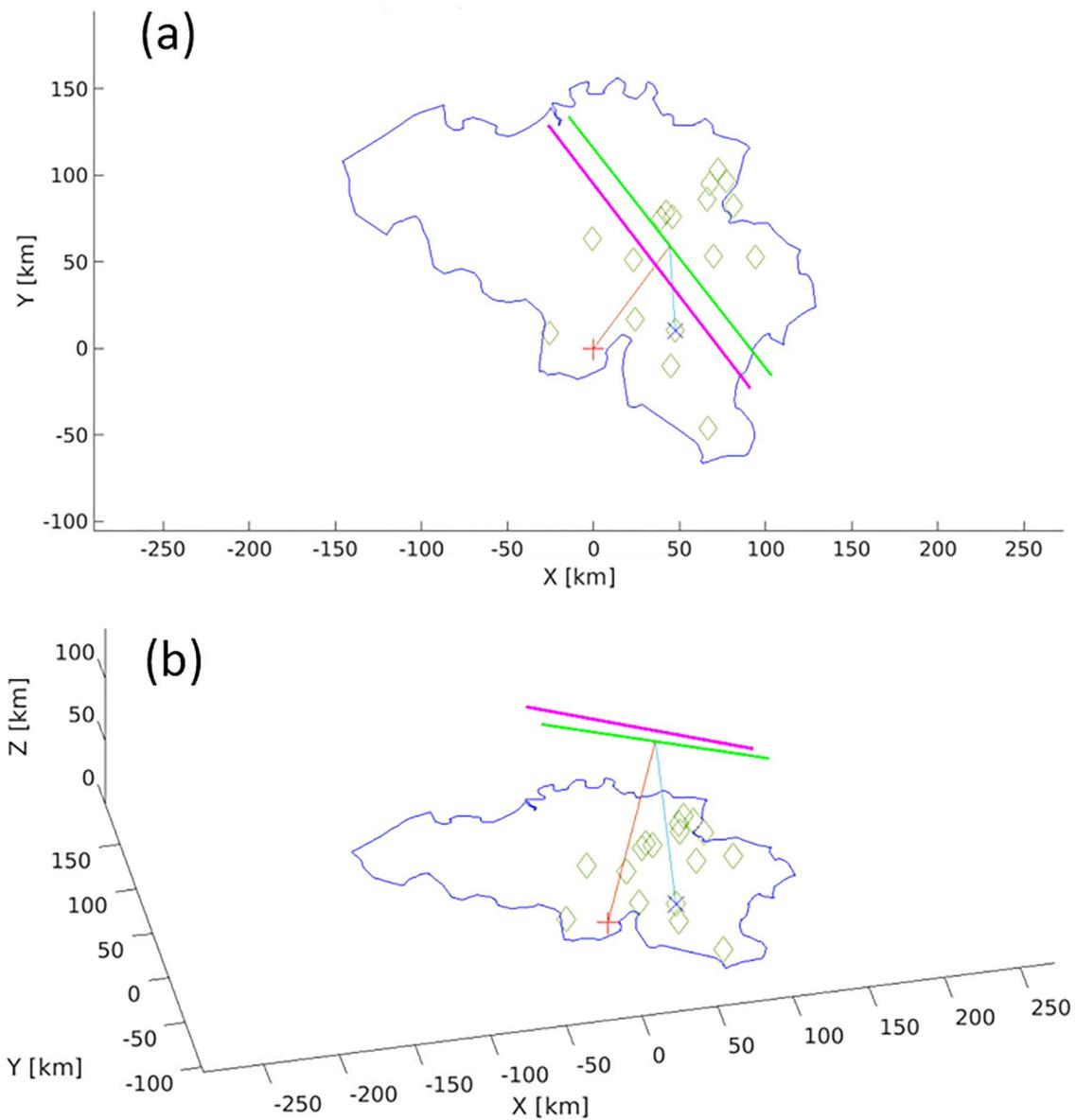
Figure 12. Example of result obtained for CAMS trajectory 79 using Method 1: (a) Projected view in the horizontal plane. (b) 3D view. The green line is the CAMS trajectory. The blue cross is the reference station (Humain). The red plus is the transmitter (Dourbes). The light green diamonds are the stations used for the BRAMS reconstruction. The orange and light blue line represent respectively the radio wave path from the transmitter to Humain specular point, and the radio wave path from this specular point to the receiver in Humain. The purple line is the reconstructed trajectory with the BRAMS signals. The blue line represents the Belgium border.

straightforward. Nonetheless, the beginning points detected by CAMS are around the same altitude as the specular points detected by BRAMS ($80-120$ km), so that we decide to compare the BRAMS constant speed with the velocity output by CAMS in $t = 0$.

An example of trajectory reconstruction with Method 1 is shown in Figure 12. This plot presents the projected CAMS trajectory 79 as well as the reconstructed one in the horizontal XY plane and in a 3D frame, where coordinates X, Y, and Z are given in a local Cartesian frame centered on the Dourbes transmitter. Seventeen BRAMS receivers are used to perform the trajectory reconstruction. Despite that the location of Humain specular point is off by about 22 km, the velocity is accurate within 6% of the CAMS data (39.65 km/s instead of 41.72 km/s), and the inclination is off by less than 0.6°.

Figure 13 presents the reconstruction results obtained for trajectory 79, but using Method 2. Since the direction of the reflection point is constrained via equations including the interferometer data, it is now better retrieved and
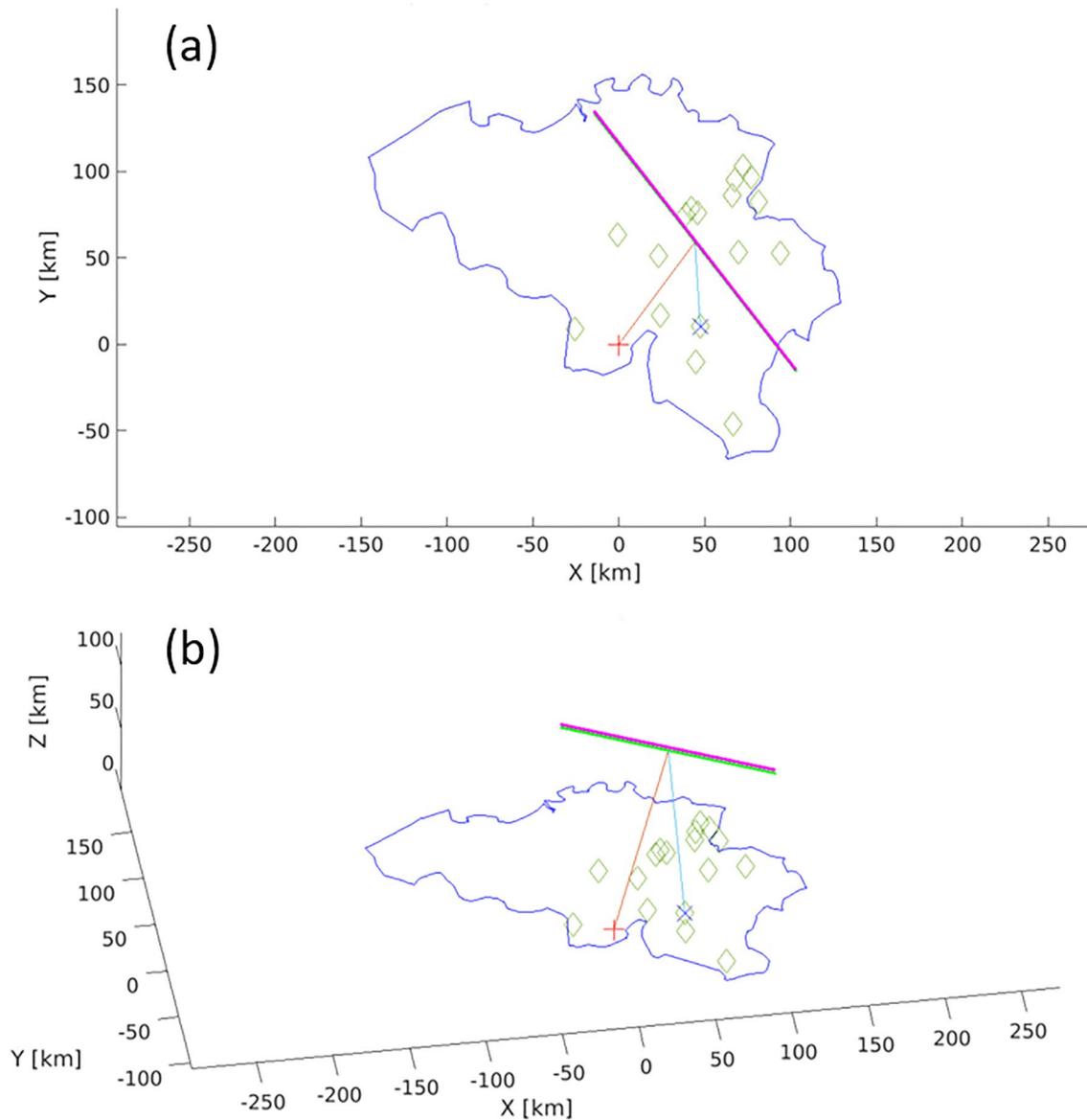
Figure 13. Example of result obtained for CAMS trajectory 79 using Method 2. The panels, lines and markers are the same as in Figure 12.

this helps greatly the reconstruction of the trajectory. The altitude of the reflection point becomes much more accurate with an error of less than 2 km. The velocity direction is accurate to 0.2° and the speed (41.07 km/s) is very close to the 41.72 km/s measured by CAMS.

Table 2 compares the number of BRAMS receivers detecting exploitable echoes for each of the 10 CAMS trajectories, and gives the reconstructed angles in the horizontal plane and the inclination angles obtained with Method 1 and 2. As it could be expected from the uncertainty quantification campaign of Section 3.3, Method 1 is not able to retrieve accurate vertical inclinations and positions systematically, due to its inherent ill-conditioned nature. It offers nonetheless good information on the orientation in the horizontal plane.

Also in agreement with our uncertainty quantification results, the horizontal angles reconstructions are within the 2° uncertainty of CAMS with both methods 1 and 2, except for meteoroids which are fast and whose trajectories are inclined with respect to the horizontal plane (in particular trajectory 773 which combines a high-speed meteoroid with a large inclination angle). This phenomenon can be explained because, as the meteoroid enters the atmosphere faster, it spends less time in the observable region of BRAMS (i.e., altitudes roughly between 80 and 120 km). Thus, the time delays between the exploitable specular points tend to be smaller. As a result, errors

Table 2
Comparison of BRAMS Reconstructions With Methods 1 and 2 and CAMS Trajectories

No.	Echoes	$\Delta\alpha_{XY,1}$ (°)	$\Delta\alpha_{XY,2}$ (°)	$\Delta\alpha_1$ (°)	$\Delta\alpha_2$ (°)
79	17	0.56	0.09	1.45	0.16
105	13	1.70	1.44	8.69	2.02
188	6	0.13	0.09	7.49	0.32
282	6	0.43	1.47	37.19	1.93
477	17	0.53	0.75	24.95	1.43
532	8	0.18	0.11	16.77	0.52
536	8	2.25	0.81	22.99	1.46
598	19	2.44	1.29	8.79	3.32
709	11	2.67	2.13	3.38	1.48
773	12	4.21	2.89	20.67	1.76

Note. $\Delta\alpha_{XY,i}$ is the difference between the angles in the horizontal plane reconstructed by CAMS and the method i using BRAMS data. $\Delta\alpha_i$ is the difference between the inclination angles reconstructed by CAMS and the method i using BRAMS data.

on the identification of the specular point location at each receiver lead to larger errors on the measured time delays. As the trajectory is further inclined, this phenomenon is amplified. In this case, the distance between the specular points (and thus the time delays for a given speed) is indeed smaller than if the trajectory is more horizontal. Similarly, high speeds and large inclinations also lead to high deceleration rates, making the constant speed model less accurate.

This observation is further reinforced by looking at the values of $\Delta\alpha_1$. Indeed, the only cases for which the inclination angle reconstruction is accurate enough with Method 1 are trajectories 79 and 105. These two meteors have either a higher number of exploitable echoes or a lower speed compared to the trajectories with larger reconstruction errors. The trajectory inclination, the meteor velocity and the number of echoes with a sufficient SNR are thus important variables which condition the reachable accuracy of the trajectory reconstruction.

Table 3 summarizes the reconstruction results obtained with Method 2 on the 10 CAMS trajectories. We can see that the velocity retrieved by our algorithm is always within the 10% error margin of the one given by CAMS. Regarding the inclination, we are always within the 2° accuracy range of CAMS, except for trajectory 598, which is the meteor with the largest velocity. For the altitude of the specular point, the results are in a lesser agreement as they are contained within ∼10 km of the value given by CAMS (except for trajectory 536, which is at 21.91 km). It is interesting to note a similar trend as before: trajectories with a high speed and inclination (e.g., trajectories 536, 709, and 773) are particularly difficult to reconstruct.

The results given in Table 3 have been obtained with Equation 17. If one has better knowledge about the quality of the data at their disposal (for instance, very good interferometric data compared to less accurate time delays measurements), one could think of giving more weight to the elevation and azimuth terms of this target objective. This might improve the altitude determination of the specular points (since the interferometer gives the direction of one specular point), but this could also deteriorate the velocity reconstruction (as it is mainly driven by the contribution of the time delays).

Table 3
Comparison of BRAMS Reconstructions With Method 2 and CAMS Trajectories

No.	ϵ (°)	V_{CAMS} (km/s)	V_{BRAMS} (km/s)	$\frac{V_{BRAMS} - V_{CAMS}}{V_{BRAMS}}$ [%]	ΔZ_H (km)	$\Delta\alpha$ (°)
79	17.72	41.72	41.07	−1.58	1.98	0.16
105	18.16	41.55	40.60	−2.34	7.79	2.02
188	11.04	29.74	28.39	−4.75	4.66	0.32
282	24.58	40.59	41.32	1.77	6.75	1.93
477	30.01	61.33	62.56	1.97	10.24	1.43
532	16.14	42.79	41.41	−3.33	7.04	0.52
536	23.69	65.07	70.13	7.21	21.91	1.46
598	4.29	70.44	71.79	1.88	8.42	3.32
709	45.96	63.70	65.96	3.43	8.58	1.48
773	52.35	65.78	71.49	7.99	0.39	1.76

Note. The second and third columns give the complement of the zenith angle ϵ and the speed of the meteoroid retrieved by CAMS at their first detection point V_{CAMS}. The fourth column gives the speed of the meteoroid retrieved by BRAMS V_{BRAMS}. The relative errors in terms of velocity, Humain specular point altitude as well as inclination angle (also given in Table 2) are shown in the last three columns.

Let us finally note that this comparison with optical data raises a question regarding the nature of the echo reflections. Indeed, optical systems tend to observe meteors of larger size than radio systems, since they need to be bright enough (the limiting magnitude of CAMS is +5 according to Jenniskens et al. (2021)) in order to be detected. As a result, the selected BRAMS echoes corresponding to the 10 CAMS trajectories are sometimes overdense or transitional. In that case, the specularity often holds as the amplitude rise of the meteor echo is not affected, but creation of secondary reflection points sometimes appear due to the distortion of the meteor trail through wind shear (Wislez, 2006).

6. Conclusion and Perspectives

In this work, we solved for the first time the general CW forward scatter trajectory reconstruction problem through a nonlinear optimization approach. We studied how the uncertainties on the time delays between meteor echoes at several radio stations impact the reconstruction accuracy of the meteoroid trajectory and speed. Method 1 (using the time delays only) appeared to be strongly ill-conditioned while interferometric data brought by Method 2 alleviated this very high sensitivity to the inputs. We implemented the data processing workflow from the acquisition of the raw signals at the receivers to the reconstructed trajectory. We finally compared our results with data coming from the optical CAMS-BeNeLux network.

Since Method 1 is the only approach that can be applied to all archived BRAMS data, its development and improvement are crucial. However, because of its ill-conditioning, it cannot be used systematically as it gives large errors in terms of specular point position and inclination angle on most trajectories. Therefore, we are currently extending the pre-t_0 phase approach described for backscatter radars in Mazur et al. (2020). This technique uses the phase of the signal before the specular point in order to retrieve the velocity of the meteoroid. It provides two important benefits. On the one hand, it further constrains the trajectory solver by adding extra inputs, thus reducing the sensitivity of the output trajectory on the input time delays. On the other hand, it allows to get some insight on the deceleration of the meteoroid during its upper atmosphere travel.

More generally, deceleration models will be introduced in the solver described in this paper, even without the extra information coming from the pre-t_0 phase. Depending on the distribution of time delays, a constant velocity can provide good fits for a meteoroid with slight deceleration by using a velocity in the middle of the region observed by the BRAMS receivers, rather than the start velocity. Other possibilities such as linear and exponential velocity models will also be tested.

We have shown that Method 2 gives more accurate results. Unfortunately, it is not applicable to the majority of past data since it requires to have at least 3 stations detecting the same meteor as the interferometer, which does not systematically happen because of the specularity condition. We have also demonstrated that increasing the number of receiving stations detecting the same meteoroid decreases the impact of measurement errors on the quality of the reconstruction. Therefore, two priorities are to build a second interferometer in the north of Belgium (where there is already a dense cluster of BRAMS receiving stations, see Figure 1) and to create clusters of radio stations around the existing interferometric station in Humain.

In parallel, the BRAMS network continues to develop. A technical description will be published shortly, also tracing its evolution over time. This future paper will also describe the trade-offs between BRAMS and other existing systems, notably in terms of area coverage, cost and data quality. In addition to the creation of receiving stations clusters and the building of a new interferometer, the use of phase coding on the transmitted CW signal (Vierinen et al., 2016) would in principle allow us to obtain the range or total distance traveled by the wave between the transmitter and the receivers. It has been shown (Lamy et al., 2021) that this extension of Method 1 would greatly facilitate the trajectory reconstruction problem.

Data Availability Statement

Version 1.1 of the BRAMS trajectories package, used for the reconstruction of meteoroid trajectories with the time delays at the BRAMS receiving stations, is preserved at https://doi.org/10.5281/zenodo.7686085, available via Creative Commons Attribution 4.0 International and developed openly at https://gitlab.aeronomie.be/ae/brams/bramstrajectories (Balis, 2023).

References

Anciaux, M., Lamy, H., Martinez Picar, A., Calders, S., Calegaro, A., Ranvier, S., & Verbeeck, C. (2020). The BRAMS receiving station v2.0. In U. Pajer, J. Rendtel, M. Gyssens, & C. Verbeeck (Eds.), *Proceedings of the International Meteor Conference, Bollmannsruh, Germany, 3–6 October 2019* (pp. 39–42).

Baggaley, W. J., Bennett, R. G. T., Steel, D. I., & Taylor, A. D. (1994). The Advanced Meteor Orbit Radar facility—AMOR. *The Quarterly Journal of the Royal Astronomical Society*, *35*, 293.

Balis, J. (2023). BRAMS trajectories package (version 1.1) [Software]. Zenodo. https://doi.org/10.5281/zenodo.7686085

Boyd, S., & Vandenberghe, L. (2004). *Convex optimization*. Cambridge University Press. https://doi.org/10.1017/CBO9780511804441

Cevolani, G., & Pupillo, G. (2009). Ground-based radio observations to probe the ozone content in the meteor region. *Annals of Geophysics*, *46*(2). https://doi.org/10.4401/ag-3399

Chau, J. L., Urco, J. M., Vierinen, J. P., Volz, R. A., Clahsen, M., Pfeffer, N., & Trautner, J. (2019). Novel specular meteor radar systems using coherent MIMO techniques to study the mesosphere and lower thermosphere. *Atmospheric Measurement Techniques*, *12*(4), 2113–2127. https://doi.org/10.5194/amt-12-2113-2019

Froncisz, M., Brown, P., & Weryk, R. J. (2020). Possible interstellar meteoroids detected by the Canadian Meteor Orbit Radar. *Planetary and Space Science*, *190*, 104980. https://doi.org/10.1016/j.pss.2020.104980

Hajduková, M., Jr., Kornoš, L., & Tóth, J. (2014). Frequency of hyperbolic and interstellar meteoroids. *Meteoritics & Planetary Sciences*, *49*(1), 63–68. https://doi.org/10.1111/maps.12119

Harris, F. (1978). On the use of windows for harmonic analysis with the discrete Fourier transform. *Proceedings of the IEEE*, *66*(1), 51–83. https://doi.org/10.1109/PROC.1978.10837

Jacchia, L., Verniani, F., & Briggs, R. E. (1967). An analysis of the atmospheric trajectories of 413 precisely reduced photographic meteors. *Smithsonian Contributions to Astrophysics*, *10*, 1–139. https://doi.org/10.5479/si.00810231.10-1.1

Jacobs, E., & Ralston, E. W. (1981). Ambiguity resolution in interferometry. *IEEE Transactions on Aerospace and Electronic Systems, AES*, *17*(6), 766–780. https://doi.org/10.1109/TAES.1981.309127

Jeanne, S. (2020). Méthode d'analyse statistique appliquée au réseau d'observation européen des météores FRIPON (Theses). *Université Paris Sciences et Lettres*.

Jenniskens, P., Gural, P., Dynneson, L., Grigsby, B., Newman, K., Borden, M., et al. (2011). CAMS: Cameras for allsky meteor surveillance to establish minor meteor showers. *Icarus*, *216*(1), 40–61. https://doi.org/10.1016/j.icarus.2011.08.012

Jenniskens, P., Lauretta, D. S., Towner, M. C., Heathcote, S., Jehin, E., Hanke, T., et al. (2021). Meteor showers from known long-period comets. *Icarus*, *365*, 114469. https://doi.org/10.1016/j.icarus.2021.114469

Jenniskens, P., Nénon, Q., Albers, J., Gural, P., Haberman, B., Holman, D., et al. (2016). The established meteor showers as observed by CAMS. *Icarus*, *266*, 331–354. https://doi.org/10.1016/j.icarus.2015.09.013

Jones, J., Brown, P., Ellis, K., Webster, A., Campbell-Brown, M., Krzemenski, Z., & Weryk, R. (2005). The Canadian Meteor Orbit Radar: System overview and preliminary results. *Planetary and Space Science*, *53*(4), 413–421. https://doi.org/10.1016/j.pss.2004.11.002

Jones, J., Webster, A. R., & Hocking, W. K. (1998). An improved interferometer design for use with meteor radars. *Radio Science*, *33*(1), 55–65. https://doi.org/10.1029/97RS03050

Karmarkar, N. K., & Ramakrishnan, K. G. (1991). Computational results of an interior point algorithm for large scale linear programming. *Mathematical Programming*, *52*(1–3), 555–586. https://doi.org/10.1007/bf01582905

Kastinen, D., & Kero, J. (2022). Radar analysis algorithm for determining meteor head echo parameter probability distributions. *Monthly Notices of the Royal Astronomical Society*, *517*(3), 3974–3992. https://doi.org/10.1093/mnras/stac2727

Lamy, H., Anciaux, M., Ranvier, S., Calders, S., Gamby, E., Martinez Picar, A., & Verbeeck, C. (2015). Recent advances in the BRAMS network. In *Proceedings of the International Meteor Conference, Mistelbach, Austria, 27–30 August 2015* (pp. 171–175).

Lamy, H., Balis, J., & Anciaux, M. (2021). Reconstructing meteoroid trajectories using BRAMS data. *WGN, Journal of the International Meteor Organization*, *49*(6), 195–200.

Lamy, H., & Tétard, C. (2016). Retrieving meteoroids trajectories using BRAMS data: Preliminary simulations. In A. Roggemans, & P. Roggemans (Eds.), *Proceedings of the International Meteor Conference, Egmond, the Netherlands, 2–5 June 2016* (pp. 143–147).

Lamy, H., Tétard, C., Anciaux, M., Ranvier, S., Picar, A. M., Calders, S., & Verbeeck, C. (2018). First observations with the BRAMS radio interferometer. In M. Gyssens, & J.-L. Rault (Eds.), *Proceedings of the International Meteor Conference, Petnica, Serbia, 21–24 September 2017* (pp. 132–137).

Markkanen, J., Lehtinen, M., & Landgraf, M. (2005). Real-time space debris monitoring with EISCAT. *Advances in Space Research*, *35*(7), 1197–1209. (Space Debris). https://doi.org/10.1016/j.asr.2005.03.038

Mazur, M., Pokorný, P., Brown, P., Weryk, R. J., Vida, D., Schult, C., et al. (2020). Precision measurements of radar transverse scattering speeds from meteor phase characteristics. *Radio Science*, *55*(10), e2019RS006987. https://doi.org/10.1029/2019RS006987

McKinley, D. (1961). *Meteor science and engineering*. McGraw-Hill. Retrieved from https://books.google.be/books?id=BSAIAQAAIAAJ

Nedeljković, S. (2006). Meteor forward scattering at multiple frequencies. In L. Bastiaens, J. Verbert, J.-M. Wislez, & C. Verbeeck (Eds.), *Proceedings of the International Meteor Conference, Oostmalle, Belgium, 15–18 September 2005* (pp. 16–24).

Nuttall, A. (1981). Some windows with very good sidelobe performance. *IEEE Transactions on Acoustics, Speech, and Signal Processing*, *29*(1), 84–91. https://doi.org/10.1109/TASSP.1981.1163506

Roggemans, P., Johannink, C., & Breukers, M. (2016). Status of the CAMS-BeNeLux network. In *Proceedings of the International Meteor Conference, Egmond, the Netherlands, 2–5 June 2016* (pp. 254–260).

Savitzky, A., & Golay, M. J. E. (1964). Smoothing and differentiation of data by simplified least squares procedures. *Analytical Chemistry*, *36*(8), 1627–1639. https://doi.org/10.1021/ac60214a047

Schult, C., Stober, G., Janches, D., & Chau, J. L. (2017). Results of the first continuous meteor head echo survey at polar latitudes. *Icarus*, *297*, 1–13. https://doi.org/10.1016/j.icarus.2017.06.019

Smith, J. O. (2011). *Spectral audio signal processing*. W3K.

Smith, S. (2013). Chapter 16—Windowed-sinc filters. In *Digital signal processing: A practical guide for engineers and scientists* (pp. 285–296). Newnes.

Stober, G., & Chau, J. L. (2015). A multistatic and multifrequency novel approach for specular meteor radars to improve wind measurements in the MLT region. *Radio Science*, *50*(5), 431–442. https://doi.org/10.1002/2014RS005591

Vierinen, J., Chau, J. L., Pfeffer, N., Clahsen, M., & Stober, G. (2016). Coded continuous wave meteor radar. *Atmospheric Measurement Techniques*, *9*(2), 829–839. https://doi.org/10.5194/amt-9-829-2016

Whipple, F. L., & Jacchia, L. G. (1957). Reduction methods for photographic meteor trails. *Smithsonian Contributions to Astrophysics*, *1*, 183–206.

Wislez, J.-M. (2006). Meteor astronomy using a forward scatter set-up. In C. Verbeeck & J.-M. Wislez (Eds.), *Proceedings of the Radio Meteor School, Oostmalle, Belgium, 10–14 September 2005* (pp. 84–106).